https://doi.org/10.1016/j.ultras.2020.106233

A Reverse Time Migration-based Multistep Angular Spectrum Approach for Ultrasonic Imaging of Specimens with Irregular Surfaces

Xiongbin Yang [a], Kai Wang [a], Yanfeng Xu [a], Lei Xu [a], Wenxiang Hu [b], Hao Wang [b], Zhongqing Su [a*]

[a] Department of Mechanical Engineering

The Hong Kong Polytechnic University, Kowloon, Hong Kong SAR

[b] Institute of Acoustics

Tongji University, Shanghai, 200092, P. R. China

Submitted to *Ultrasonics*

(initially submitted on 22nd May 2020; revised and re-submitted on 8th July 2020)

* To whom correspondence should be addressed. Tel.: +852-2766-7818, Fax: +852-2365-4703, Email: Zhongqing.Su@polyu.edu.hk (Prof. Zhongqing SU, *PhD*)

Abstract

We develop a new ultrasonic imaging framework for non-destructive testing of an immersed specimen featuring an irregular top surface and demonstrate its capability of accurately depicting the lower surfaces of multiple damages hidden in the specimen. Central to the framework is a multistep angular spectrum approach (ASA), via which the forward propagation wavefields of wave sources and backward propagation wavefields of the received wave signals are calculated. Upon applying a zero-lag cross-correlation imaging condition of reverse time migration (RTM) to the obtained forward and backward wavefields, the image of the specimen with an irregular surface can be reconstructed, in which hidden damages, if any and regardless of quantity, are visualized. The effectiveness and accuracy of the framework are examined using numerical simulation, followed with experiment, in both of which multiple side-drilled holes, at different locations in aluminum blocks with various irregular surfaces, are characterized. Results have proven that multiple damages in a specimen with an irregular surface can be individually localized, and the lower surface of each damage can further be imaged accurately, thanks to the RTM-based algorithm in which multiple wave reflections from the specimen bottom are taken into wavefield extrapolation. The proposed imaging approach presents higher computational efficiency, compared to conventional RTM, and enhanced imaging contrast over prevailing total focusing methods.

***Keywords*:** reverse time migration (RTM); angular spectrum approach (ASA); irregular surface; ultrasonic imaging; nondestructive testing (NDT)

1. Introduction

Ultrasonic imaging, in conjunction with the use of phased arrays, has gained its prominence in nondestructive testing (NDT) and demonstrated its effectiveness in characterizing invisible defect or damage in specimens [1-4]. During implementation, the imaging algorithm is a predominant factor governing the accuracy and resolution that a reconstructed image can deliver. The prevailing imaging algorithms today have proven capacity of inspecting a specimen with a flat surface which is either in parallel or oblique to the surface of the phased array. Nevertheless, these algorithms often fail when they are extended to the specimens with non-planar surfaces, irrespective of the fact that the non-planar surfaces are ubiquitous in engineering practice such as weld-caps, molded components and pipelines. To circumvent such deficiency that most ultrasonic imaging algorithms may encounter, conventional phased arrays are retrofitted to possess curved surfaces that are adaptive to non-planar specimens, as typified by the flexible array [5,6] and membrane-coupled conformable array [7]; alternatively, the ultrasonic scanning can be implemented in a contactless manner via water immersion for example, whereby to minimize energy loss when ultrasonic waves traverse from a phased array to the specimen [8,9].

In addition to the challenge from the non-planar surfaces, the hidden damage in a solid also introduces extra obstacle to ultrasonic imaging. To gauge a damage deeply hidden, sophisticated imaging algorithms have been developed. Representatively, using an improved imaging algorithm originated from a total focusing method (TFM) [10-12] which combines the full matrix capture (FMC) information [13] and a virtual source aperture approach, a dual-layered medium with a complex interface was imaged with good resolution [14-17]. Nevertheless, TFM-based imaging is computationally expensive in general, because it demands intensive calculation of time-of-flights (ToFs) of wave propagation along different paths, based on the Fermat principle such as the spatial discrete searching or numerical iteration. Even though, the image resolution tends to be compromised as the specimen depth increases – a consequence of the exponentially increased wave attenuation as the probing wave penetrates the specimen. Moreover, in a TFM-based method, multiple wave reflections from the specimen bottom may considerably complicate wave signals and lower signal-to-noise ratio, resulting in artifacts in reconstructed images.

Reverse time migration (RTM), originating from seismic imaging [18], has consolidated its popularity in ultrasonics-based NDT in recent years. Yuan *et al* [19-22] applied RTM to image and localize damage in a thin plate. He *et al* [23-25] presented RTM with a normalized zero-lag cross-correlation imaging condition to image and quantify multiple sites of damage in isotropic plate. Gao *et al* [26] proposed a mixed method by combining the time reverse algorithm with RTM, via which an internal damage in a multi-layered medium was detected and visualized accurately. Anderson *et al* [27] designed a subtle time reverse mirror to implement the RTM-driven imaging for localizing disbonding in a bounded aluminum plate. In these paradigms, the RTM-based imaging is manipulated with a postulation that when a receiver wavefield is propagated backward from the receiver in the time domain, the wave components reflected from the internal damage will, in principle, focus at the location of the damage – a method based on the wavefield extrapolation of full wave equation. RTM-driven imaging mitigates, to a certain degree, the abovementioned deficiency of TFM-based imaging (namely, the deeper the damage in a specimen the lower the imaging precision it will be), by improving the imaging contrast for a damage at a greater depth in the specimen [10-12]. That is because RTM-based imaging makes use of the multiple wave reflections from the specimen bottom which carry rich information on the internal damage, rather than discarding the multiple reflections as a conventional TFM-based imaging approach does.

With such a merit, RTM-based imaging has been proven effective in characterizing circular tendon ducts in concrete media [28], and vertical slots or irregulated shaped notches in metallic blocks [29-30].

The underlying principle of RTM-based imaging is the simultaneous extrapolation of forward propagation of wave sources and backward propagation of the received wave signals. In most circumstances, the simultaneous extrapolation can be implemented through numerical means such as finite difference time-domain methods (FDTDMs) [28] or finite element methods (FEMs) [29]. However, numerical simulation usually entails full modeling in the spatial domain and computation of the entire specimen, including the coupled fluid in which the specimen is immersed. Apparently, it is highly computationally expensive and unnecessary to model and image the entire fluid–solid coupled system. Moreover, the massive computation burdens computing hardware. To mitigate demanding requirements from data storage and ROM, parallel computing techniques such as those based on CPU or advanced GPU have been exploited, with a hope to accelerate the computation of wave propagation [31]. However, it is still a daunting task to break through the computational bottleneck [32]. As a remedial measure, an analytical RTM approach [33] using fictitious sources was developed, in which the integral in wave propagation computation was substituted with approximate calculation, whereby to remarkably improve computational efficiency and reduce cost, although such a measure shows proven effectiveness only for those specimens with simple geometric features, for example a homogeneous medium with a flat top surface.

As an alternative to FDTDMs and FEMs, the angular spectrum approach (ASA) depicts wave propagation in the frequency–wavenumber domain [34], via which an acoustic source can be decomposed to the plane of angular spectrum using the Fourier transform. Notably, ASA can be extended to a curved radiator [35]. The angular spectrum is extrapolated in the depth direction of the specimen, and thus the sound field at any depth of the specimen can be defined via the inverse Fourier transform of angular spectrum. Benefiting from the nature that the majority of calculation in ASA can be performed via Fourier transform and inverse Fourier transform, the approach in general assures higher computational efficiency compared to other numerical methods such as FDTDMs used in most RTM-based imaging. Furthermore, ASA reconstructs a wavefield locally at any depth of the specimen, rather than modeling and imaging the entire fluid–solid coupled system. Such a merit makes it possible to gauge only the local region of interest (RoI) – the vicinity in the specimen where a damage may exist, remarkably lowering computational cost and unburdening computing hardware.

Nevertheless, the conventional ASA is usually limited to modeling the propagation of a sound field in a homogeneous and isotropic medium. That is because the Fourier transform from the spatial domain to the frequency–wavenumber domain cannot be implemented at an interface on which the acoustic parameters are non-uniform along the horizontal direction in the Cartesian coordinate system. To circumvent such a problem, Belgroune *et al* [36] revamped the conventional ASA algorithm by rotating the coordinates, to model wave beam transmitted from the liquid to the solid through a plane interface. Varray *et al* [37], with consideration of wave nonlinearity and wave attenuation, investigated the second harmonic wave propagation in an inhomogeneous solid via a generalized ASA algorithm. With that, wavefields along both the horizontal and depth directions of the specimen were depicted through fractionizing the inhomogeneous layer into a series of rectangular homogeneous fragments, in each of which the conventional ASA algorithm was applied [38]. However, these methods may encounter restrictions when they are extended to a specimen featuring an irregular top surface (e.g., a curved surface), because neither the rotation of coordinates nor fractionization of the irregular surface can alter the irregular interface (between the specimen and the fluid) to a surface with uniform acoustic parameters along the horizontal direction.

In recognition of the limitations of conventional TFM, RTM and ASA, as commented in the above, a new ultrasonic imaging framework for non-destructive testing of an immersed specimen with an irregular top surface is proposed. To circumvent the incapability of conventional ASA-based imaging when it is used to tackle specimens with irregular surfaces, to which the spatial Fourier transform cannot be implemented in the horizontal direction, a multistep ASA algorithm is developed. With the multistep ASA, the forward propagation wavefields of wave sources and backward propagation wavefields of the received wave signals are calculated, which is applicable to the specimen featuring an irregular interface with the coupled fluid. With accurate depiction of the forward and backward propagation wavefields, an image of the specimen is reconstructed after applying a cross-correlation imaging condition of RTM. The proposed framework is validated via numerical simulation and experiment, in both of which multiple side-drilled holes, at different locations in aluminum blocks with various irregular surfaces, are characterized. Resolution and precision of the imaging are compared with those of conventional TFM-based imaging.

The layout of this paper is as follows: Section 2 elaborates on the proposed RTM-based multistep ASA for ultrasonic imaging, following succinct introduction to the background knowledge of RTM. A dual-layer medium – a fluid–solid coupled system with an irregular interface is discussed in Section 2, for illustrating the principle of the proposed approach, which is verified using FEM. In Section 3, accuracy and precision of the multistep ASA-based imaging are examined experimentally. Two aluminum blocks with irregular surfaces are prepared, in which multiple side-drilled holes are introduced as multiple hidden damages. Section 4 compares the ASA-based algorithm against TFM in terms of the imaging quality. Key observations and conclusions from this study are recapped in the last section.

2. RTM-based Multistep ASA

2.1 RTM

In RTM-based imaging, the imaging conditions are applied to the forward propagation of a source signal and the backward propagation of a received signal, to reconstruct an image along the specimen depth. Both the forward and backward wave propagation in a homogeneous medium is calculated on the basis of acoustic wave equation using acoustic parameters (density, acoustic velocity, etc.) known a priori, with the assumption that the specimen is free of damage. **Figure 1** shows the schematic of wave propagation in a homogeneous solid immersed in fluid with an irregular top surface (i.e., a fluid–solid coupled system with an irregular interface) and a hidden damage, when an *N*-element linear phased array is placed in the fluid to perform ultrasonic scanning.

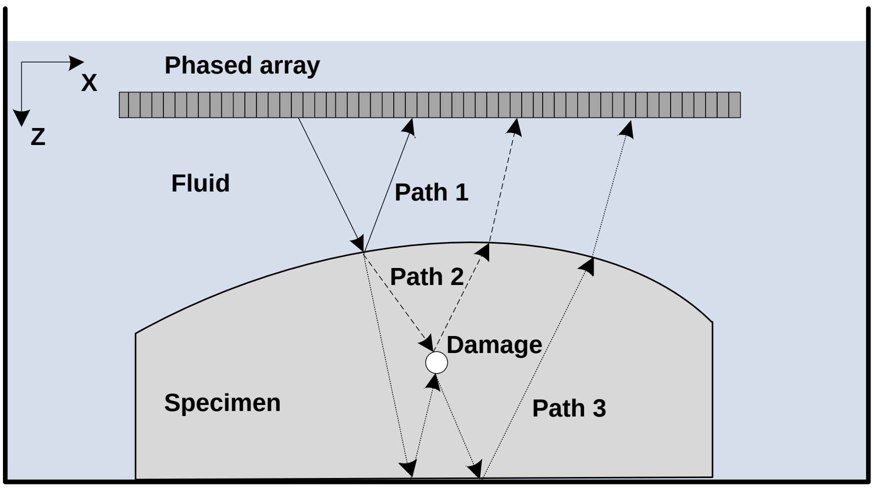

Fig. 1. Schematic of wave propagation in a fluid–solid coupled system with an irregular interface

and hidden damage, under ultrasonic inspection using a phased array

For the two-dimensional (2D) scenario shown in **Fig .1**, with (x,z) representing the Cartesian coordinates of an image pixel and t denoting the time, consider three paths of wave propagation when the n^{th} element in the phased array ($n = 1, 2, ..., N$) is triggered to emit a probing wave into the coupled system: *Path 1* – the wave is reflected directly from the upper surface of the specimen, and then captured by an element in the array; *Path 2* – the wave is incident to the specimen, reflected by the damage, and then captured by an element in the array; and *Path 3* – the wave is incident to the specimen, reflected by the specimen bottom to interact with the lower damage surface, reflected by the bottom again after wave scattering from the lower damage surface, and then captured by an element in the array. Amongst these three wave propagation paths, the wave signal along *Path 1* contributes to the spatial determination of the specimen top surface, while the signals along *Paths 2* and *3* facilitate imaging of the hidden damage. The wave signal acquisition duration, *T*, shall be sufficiently long, so that the multiple reflections from the specimen bottom along *Path 3* can be included in the captured signals.

RTM-based imaging embraces the following three key steps in sequence:

I. the wave signal excited by the n^{th} element in the phased array is propagated forward in time with material properties and medium geometrical information known *a priori*, to extrapolate the source wavefields $S_n(x,z,t)$, ($n = 1, 2, ..., N$) from the initial time (when $t = 0$) through the end of the signal acquisition (when $t = T$);
II. the received signals are reversed in time – the kernel of the RTM-based imaging; subsequently, the time-reversed signals are excited at the corresponding locations of all elements in the array, to extrapolate the receiver wavefields $R_n(x,z,T-t)$; and
III. the image of the specimen is reconstructed after the zero-lag cross-correlating the

source wavefields and the receiver wavefields under certain imaging conditions.

In this study, the zero-lag cross-correlation imaging condition in III, for all the possible pairs of source elements and receiving elements in the array, is defined as

$$I(x,z)=\sum_{n=1}^{N}\frac{\sum_{t=0}^{T}S_n(x,z,t)\cdot R_n(x,z,T-t)}{\sum_{t=0}^{T}S_n^2(x,z,t)}, \qquad (n=1,2,...,N) \tag{1}$$

where $I(x,z)$ is the image value at pixel (x,z) in the reconstructed image. To obtain the forward propagation wavefield $S_n(x,z,t)$ and backward propagation wavefield $R_n(x,z,T-t)$ in the specimen, one can use numerical methods such as FDTDMs or FEMs, with which the entire fluid–solid coupled system, including the fluid, has to be modeled and imaged. This demands extraordinarily high yet unnecessary computational cost, even though the wavefield in the fluid contributes none to characterization of damage – a major demerit that conventional RTM-based imaging has.

2.2 Multistep ASA

A multistep ASA-based imaging framework is developed, to break through the limitations of conventional RTM in tackling fluid–solid coupled media with irregular interfaces. This framework allows modeling and calculation of the wavefields in RoI only, rather than the entire coupled system. Furthermore, it circumvents the shortcoming of the conventional ASA (namely, the extrapolation of wavefield can only be fulfilled when the interface possesses uniform acoustic parameters in the horizontal direction, and it cannot be extended to a solid with an irregular surface).

With the assumption that (i) wave reflections from the top surface of the fluid and from the phased array surface are not taken into account, and (ii) the mode conversion in wave propagation is neglected, due to the weakness in energy of the converted shear wave mode, and only the longitudinal wave is investigated. The model for extrapolating wavefields is illustrated schematically in **Fig. 2**. A twofold calculation process is proposed for wavefield extrapolation: (i) wave propagation in the fluid is ascertained to obtain the wavefields at the fluid–solid interface, as detailed in Section 2.2.1; (ii) the obtained wavefields at the interface are then treated as incident waves to emit into the solid, and with that the wavefields in the solid are extrapolated, Section 2.2.2.

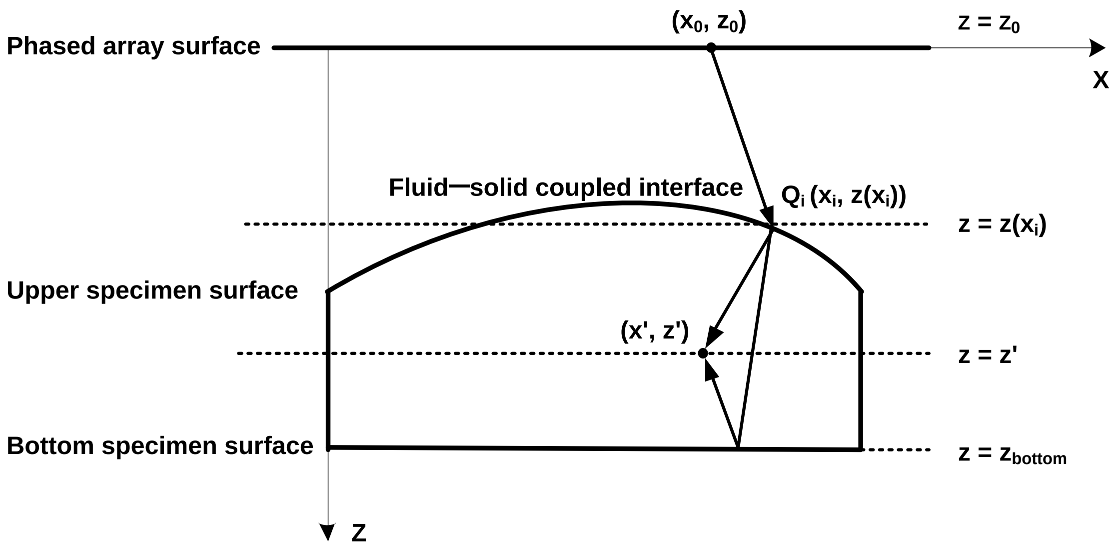

Fig. 2. A 2D model for wavefield extrapolation in a fluid–solid coupled system with an irregular interface

2.2.1. Wavefields in Fluid and at Interface

For the fluid–solid coupled system with an irregular interface shown in **Fig. 2**, a phased array is placed in the fluid at the plane when $z = z_0$, for wave excitation and acquisition. Given that an input signal $p(t)$ is produced by a source element in the phased array at (x_0, z_0), the

Fourier modality of the acoustic pressure distribution, $P(x,z,f)$, at the initial plane when $z=z_0$ can be expressed as

$$P(x,z_0,f)=P(f)\cdot\delta(x-x_0),\tag{2}$$

where δ signifies the Dirac function and f the frequency. $P(f)$ is the Fourier transform of $p(t)$. Subsequently, Fourier transform is re-applied to $P(x,z_0,f)$ with respect to *x*, to transform $P(x,z_0,f)$ from the spatial to the wavenumber domain, and obtain its angular spectrum, $\hat{P}(k_x,z,f)$, at the plane when $z=z_0$, which reads

$$\hat{P}(k_x,z_0,f)=P(f)e^{-ik_x x_0},\tag{3}$$

where k_x denotes sampling wavenumber along *x* direction in the spatial frequency domain, which is the same in the solid and the fluid.

Without loss of the generality, arbitrarily choose a point at the irregular interface, Q_i (here, subscript *i* denotes a parameter at the interface; $i=1,2,...,M$ where *M* stands for the total number of the discrete points selected on the interface for ASA calculation). The coordinates of Q_i, namely $(x_i,z(x_i))$, can be determined in terms of the ToF of the first echo wave (i.e., the wave propagating along *Path 1* as shown in **Fig. 1**). When the probing wave travels from the initial plane ($z=z_0$) to point Q_i, the angular spectrum of the acoustic field at the plane $z=z(x_i)$, denoted with $\hat{P}(k_x,z(x_i),f)$, can be derived by introducing a phase shift with regard to $\hat{P}(k_x,z_0,f)$, as

$$\hat{P}(k_x,z(x_i),f)=\hat{P}(k_x,z_0,f)e^{-ik_{fluid-z}(z(x_i)-z_0)},\tag{4}$$

where $k_{fluid-z}=\sqrt{k_{fluid}^2-k_x^2}$ ($k_{fluid}=2\pi f/c_{fluid}$: the wavenumber in the fluid; c_{fluid}: the velocity of wave in the fluid).

Subsequently, the transient wavefield at Q_i, viz., $p\left(x_i, z\left(x_i\right), t\right)$, can be calculated upon applying the 2D inverse Fourier transform (including a spatial inverse Fourier transform first, and then a temporal inverse Fourier transform) on $\hat{P}\left(k_x, z(x_i), f\right)$, via

$$p\left(x_i, z\left(x_i\right), t\right) = F_{2D}^{-1}\left\{\hat{P}\left(k_x, z(x_i), f\right)\Big|_{x=x_i}\right\}, \tag{5}$$

where F_{2D}^{-1} represents the 2D inverse Fourier transform.

2.2.2. Wavefields in Solid

The transient wavefield at the interface derived in the above, $p\left(x_i, z\left(x_i\right), t\right)$, is incident to the solid. Provided a damage exists in the solid at (x', z'), in **Fig. 2**, the damage scatters the incident wave via direct reflection from the plane $z = z'$ (*Path 2*) and multiple reflections from the specimen bottom (*Path 3*). In the same vein, the angular spectrum of the acoustic field at the plane $z = z'$, where the damage exists, $\hat{P}_i^{(solid)}\left(k_x, z', f\right)$, can be ascertained, using Eq. (4), as,

$$\hat{P}_i^{(solid)}\left(k_x, z', f\right) = \hat{P}\left(k_x, z(x_i), f\right)e^{-ik_{solid-z}\left(z'-z(x_i)\right)} + C\cdot\hat{P}\left(k_x, z(x_i), f\right)e^{-ik_{solid-z}\left(2z_{bottom}-z'-z(x_i)\right)}.$$

$$(\, i = 1, 2, \ldots, M\,) \tag{6}$$

In Eq. (6) the first term $\hat{P}\left(k_x, z(x_i), f\right)e^{-ik_{solid-z}\left(z'-z(x_i)\right)}$ and the second term $C\cdot\hat{P}\left(k_x, z(x_i), f\right)e^{-ik_{solid-z}\left(2z_{bottom}-z'-z(x_i)\right)}$ refer to the wavefields contributed by *Paths 2* and *3*, respectively; the superscript or subscript "*solid*" distinguishes variables in the solid from those in the fluid as used in Section 2.2.1. $k_{solid-z} = \sqrt{k_{solid}^2 - k_x^2}$ (k_{solid}: the wavenumber in the solid). C is a generalized reflection coefficient determined by the traction-free boundary condition at the specimen bottom, which can be obtained by solving Eq. (6) when the term $\sum_i \left[\hat{U}\left(k_x, z(x_i), f\right) e^{-ik_{solid-z}\left(z'-z(x_i)\right)} + C \cdot \hat{U}\left(k_x, z(x_i), f\right) e^{-ik_{solid-z}\left(2z_{bottom}-z'-z(x_i)\right)} \right]$ is zero. It is the introduction of such a coefficient in the angular spectrum calculation that makes it possible to accurately describe the lower surface of the hidden damage, in contrast with conventional imaging using TFM in which only the wave reflections from the upper surface of the damage (i.e., wave propagation along *Path 2*) are considered. Equation (6) is manipulated for each discrete point on the interface (*M* in total) to yield $\hat{P}_i^{(solid)}\left(k_x, z', f\right)$ (where $i = 1, 2, \ldots, M$), summation of which leads to the total angular spectrum $\hat{P}^{(solid)}\left(k_x, z', f\right)$, at the plane $z = z'$ (where damage exists):

$$\hat{P}^{(solid)}\left(k_x, z', f\right) = \sum_{i=1}^{M} \hat{P}_i^{(solid)}\left(k_x, z', f\right). \qquad (i = 1, 2, \ldots, M) \tag{7}$$

Subsequently, using the 2D inverse Fourier transform, the transient wavefield at the point $\left(x', z'\right)$ can be obtained, as

$$p\left(x', z', t\right) = F_{2D}^{-1}\left\{ \hat{P}^{(solid)}\left(k_x, z', f\right)\Big|_{x=x'} \right\}. \tag{8}$$

Upon applying the above multistep ASA to the excited signals and time-reversed signals, the forward and backward propagation wavefields in the solid are defined. With the wavefields, the entire solid can be imaged using RTM algorithm, in which damages, if any in the solid and regardless of the quantity, can be visualized.

2.3. Numerical Verification

To verify the RTM-based multistep ASA for ultrasonic imaging, numerical simulation is performed first, in which a 2D fluid–solid coupled system, as schematically shown in **Fig.**

3(a), is considered. The depth of the fluid and the solid is 10 mm each, with respective key acoustic parameters listed in **Table 1**, and key parameters used in ASA calculation in **Table 2**.

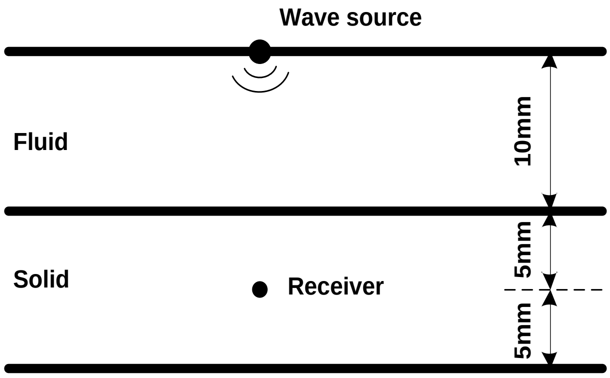

(a)

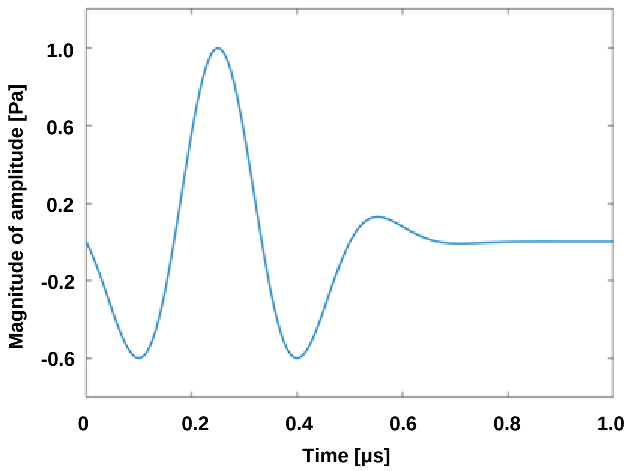

(b)

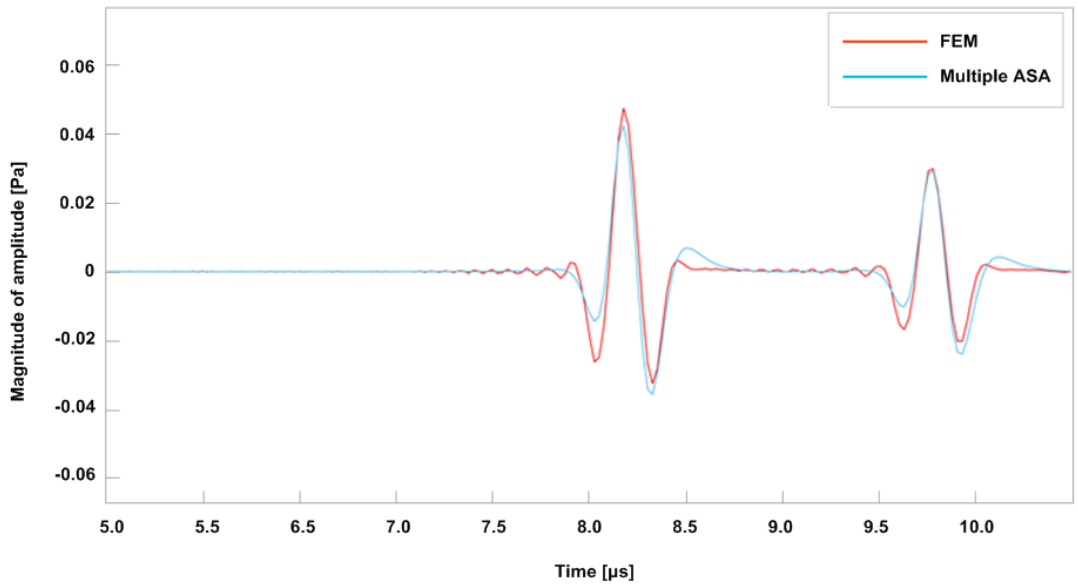

(c)

Fig. 3. (a) A simplified 2D fluid–solid coupled system for illustrating multistep ASA-based imaging; (b) excitation signal; and (c) comparison of results obtained using the proposed algorithm and using FEM

Table 1. Acoustic parameters of the fluid–solid coupled system in simulation

	fluid	solid
Velocity of wave (m/s)	1480	6300
Density (kg/m^3)	1000	2700

Table 2. Key parameters used in simulation for 2D inverse Fourier transform

Sampling frequency	80 MHz
Sampling interval of frequency	0.05 MHz
Sampling wavenumber	45 mm^{-1}
Sampling interval of wavenumber	0.005 mm^{-1}

A point-like wave source is placed at the upper boundary of the fluid to excite an acoustic wave – a 1.5-cycle hamming modulated sinusoidal tone-burst centered at 5MHz, **Fig. 3(b)**. Eight discrete points per wavelength are selected on the interface (Q_i) for multistep ASA calculation.

To verify the results obtained using multiple ASA, FEM-based modeling and simulation are performed using COMSOL Multiphysics® software. The FEM model features the same dimension along the *z* direction with that in the multistep ASA calculation, while it has a finite dimension along the *x* direction and is then applied with acoustic absorbing boundaries at both the left and right boundaries (eliminating wave reflection at boundaries). Thus, the model used in the multistep ASA calculation and the one in FEM simulation have the identical boundary conditions. The mesh size of the FEM model is 0.06 mm in the fluid and 0.24 mm in the solid. Arbitrarily choosing a point in the solid as the receiving point, as indicated in **Fig. 3(a)**, the time-series signal of the FEM-calculated wavefield at the receiving point is compared with that obtained using the multistep ASA, in **Fig. 3(c)**, to observe quantitative matching in between.

It is noteworthy that under the same computational conditions, the computing time consumed by the multistep ASA calculation is reduced drastically to 50 seconds from the 3390 seconds used by the FEM simulation.

3. Experimental Validation

The multistep ASA-based imaging framework is validated experimentally on an ultrasound testing platform (SonixTOUCH, *Ultrasonix*™). Two aluminum blocks with irregular top surfaces – one featuring a parabolic surface and the other a wavelike surface, are immersed in water for ultrasonic scanning.

3.1. Set-up and Specimens

The experimental set-up is illustrated schematically in **Fig. 4**, showing the key equipment adopted. The first specimen, Fig. 5(a), has a parabolic surface, in which four side-drilled holes (SDHs) are pre-treated, the diameter of these holes is 2.5 mm, which is prudently selected to examine the detectability of the proposed algorithm; while the second specimen, **Fig. 6(a)**, possesses a top surface of a sinusoidal profile, in which two SDHs (Ø2.5 mm each) are pre-introduced. The locations of array surface, specimen surfaces, and SDHs are indicated in **Fig. 5(a)** and **6(a)**, for two specimens.

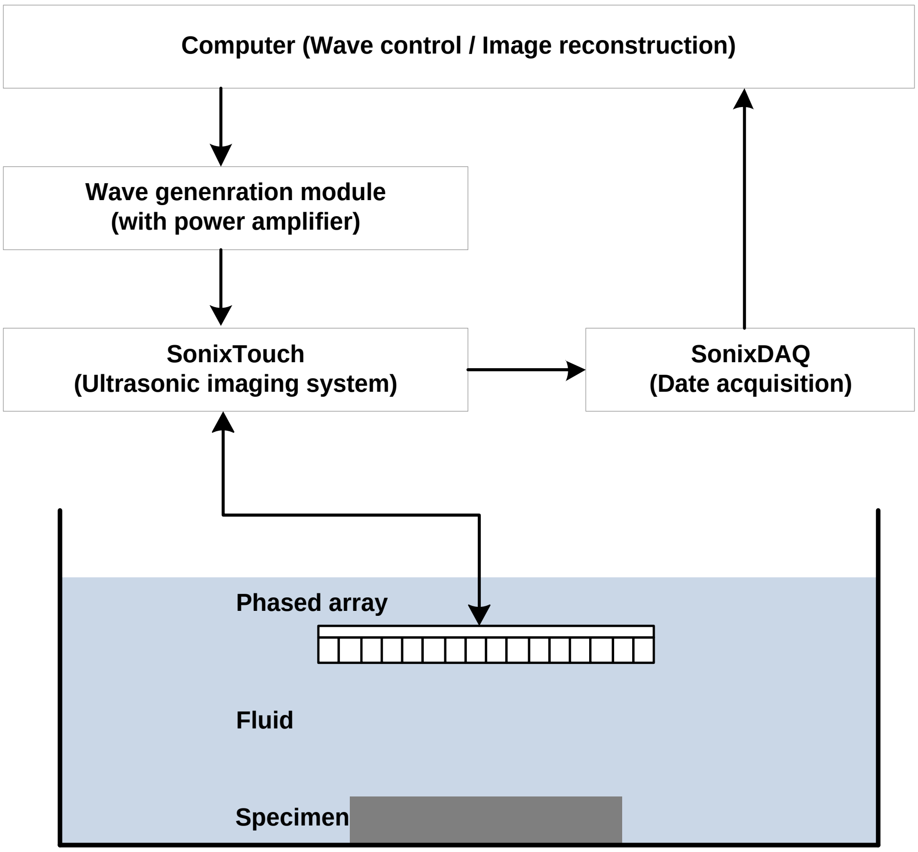

Fig. 4. Schematic of experimental set-up for validation

The respective acoustic parameters of the fluid and the two specimens remain the same as those in numerical verification, **Table 1**. A multi-channel data acquisition module (SonixDAQ, *Ultrasonix*™) is used to capture signals which renders up to 128 channels at a sampling rate of 80 MHz for each channel. A commercial array controller (SonixTOUCH, *Ultrasonix*™) regulates a linear array with a central resonance frequency of 5 MHz which comprises 128 elements (0.2698 mm in width for each element and 0.3048 mm in pitch). A 1.5-cycle Gaussian pulse is excited with the array under an applied voltage of 60 V, to generate the probing ultrasonic waves. Reflected wave signals from the specimen surface, damage, and specimen bottom are acquired with the array via fluid coupling.

3.2. Results

The surface of each specimen is first determined via a B-scan, in which only the wave propagation along *Path* 1 is considered, with results shown in **Fig. 5(b)** and **6(b)**. The identified specimen surfaces tally well with the reality. With determination of the location of the specimen surface, the transient wavefields at the specimen surface are calculated using the multistep ASA (Eq. (5)). Subsequently, these wavefields are used as the incident waves to the specimen, and the wavefields at any location throughout the entire specimen can be calculated using Eqs. (6), (7) and (8). Applied with the zero-lag cross-correlation imaging conditions as defined in Eq. (1), the image of the RoI (the region near the SDHs, namely the dotted-line-framed region in figures) can be reconstructed, shown in **Fig. 5(c)** and **6(c)**.

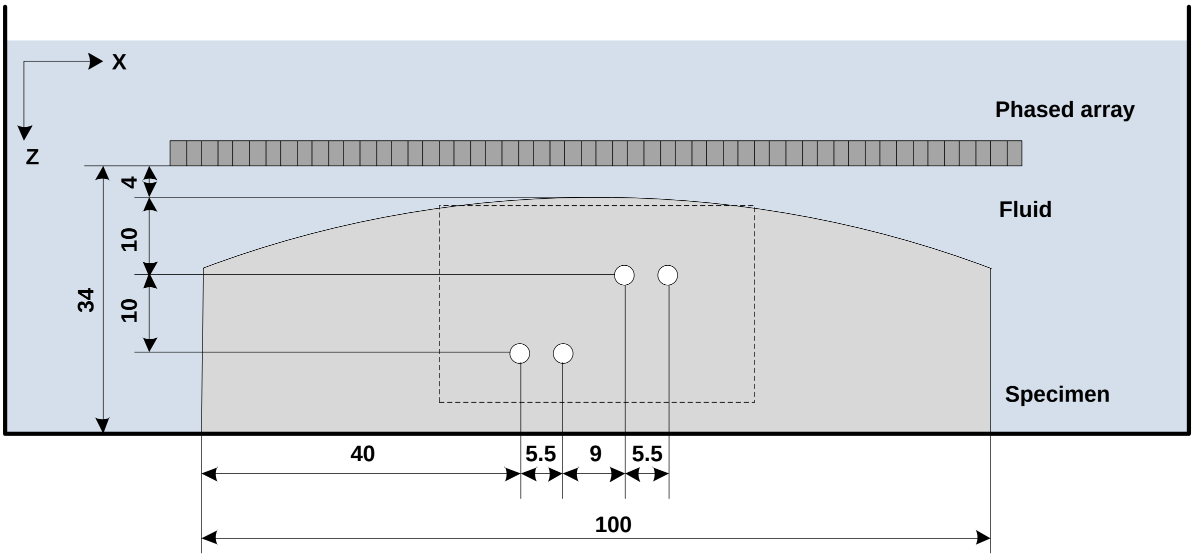
X
Z
Phased array
Fluid
Specimen
4
10
10
34
40
5.5
9
5.5
100

(a)

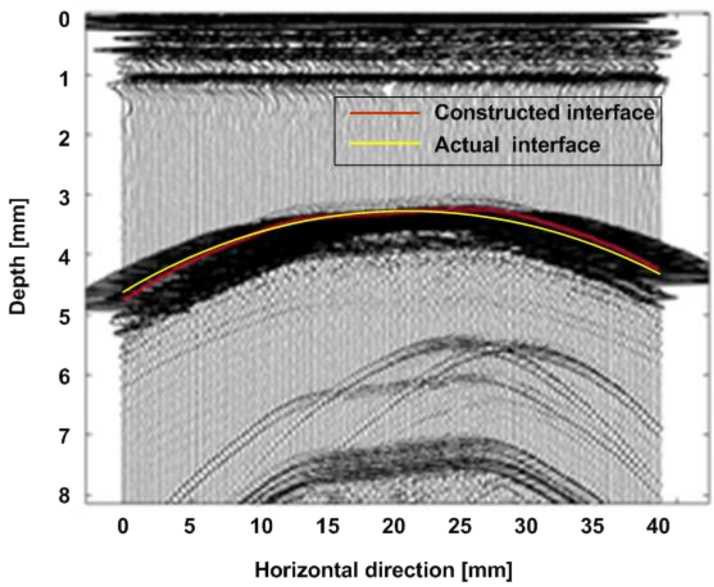
Constructed interface
Actual interface
Depth [mm]
0
1
2
3
4
5
6
7
8
0
5
10
15
20
25
30
35
40
Horizontal direction [mm]

(b)

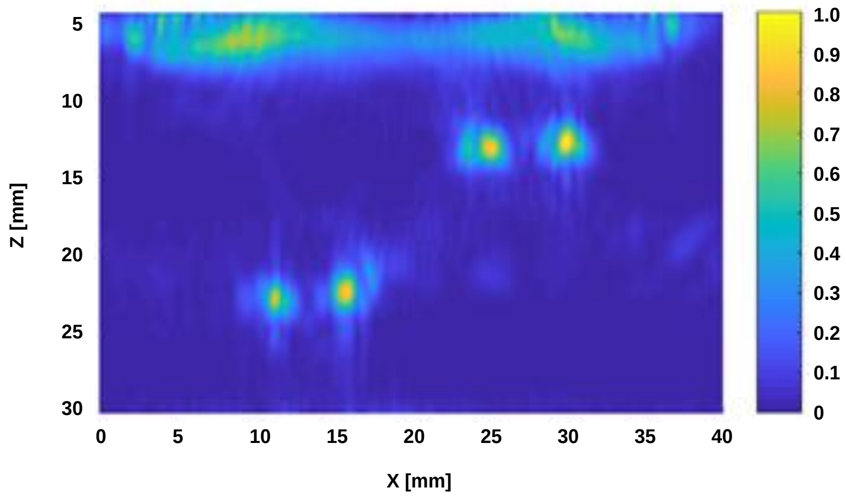

(c)

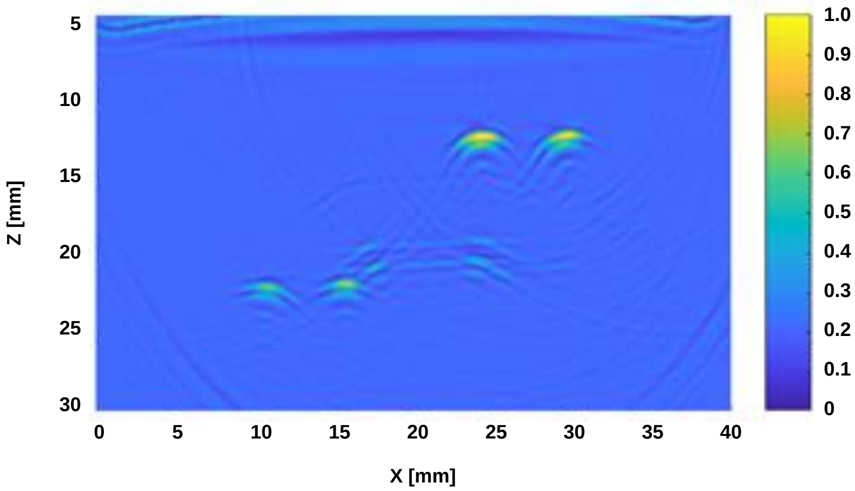

(d)

Fig. 5. (a) An aluminum block featuring a parabolic surface with four SHDs (unit: mm); (b) image of the upper part of the specimen constructed by a B-scan, for determination of specimen upper surface; (c) reconstructed image using the proposed imaging algorithm; and (d) reconstructed image using conventional TFM (for (c) and (d), *Z* axis represents the distance below the array surface which is positioned at *Z*=0; *X* axis represents the distance in RoI only (dotted-line-framed region in Fig. 5(a))

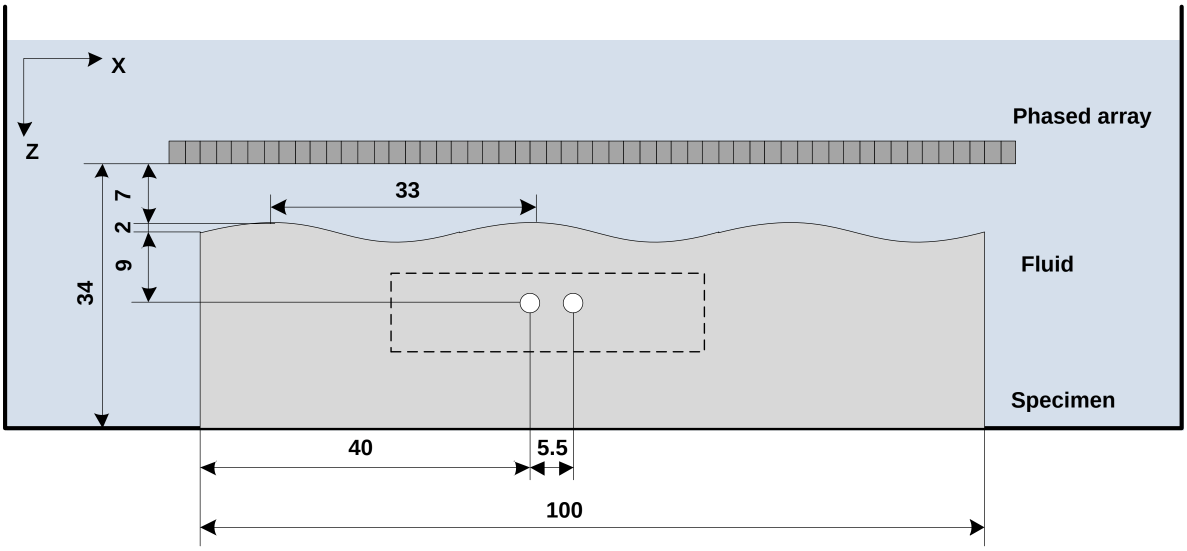
X
Z
Phased array
33
7
2
9
34
Fluid
Specimen
40
5.5
100

(a)

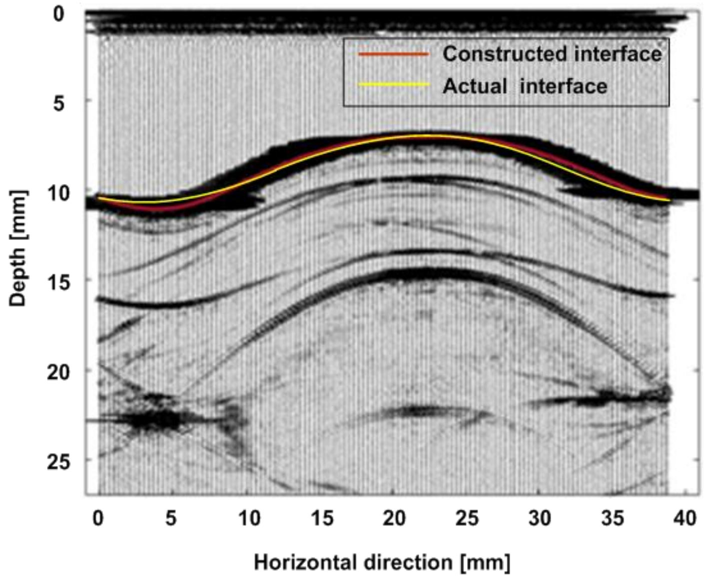
Constructed interface
Actual interface
Depth [mm]
0
5
10
15
20
25
0
5
10
15
20
25
30
35
40
Horizontal direction [mm]

(b)

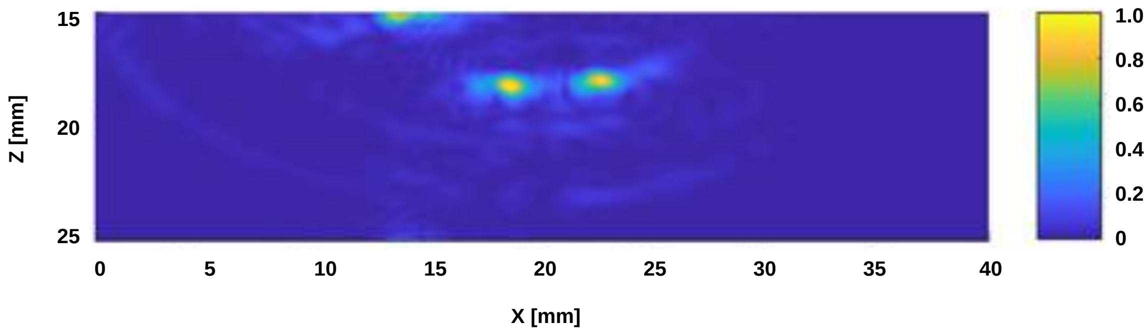
Z [mm]
15
20
25
0
5
10
15
20
25
30
35
40
X [mm]
1.0
0.8
0.6
0.4
0.2
0

(c)

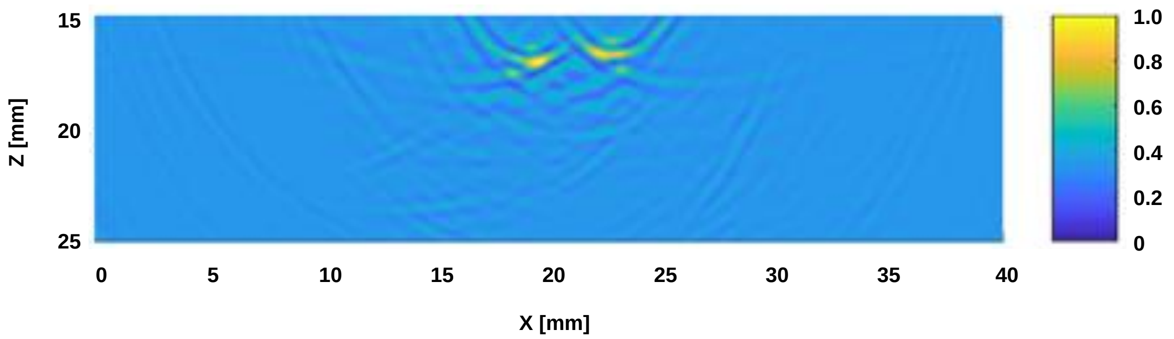

(d)

Fig. 6. (a) An aluminum block featuring a sinusoidal surface with two SHDs (unit: mm); (b) image of the upper part of the specimen constructed by a B-scan, for determination of specimen upper surface; (c) reconstructed image using the proposed imaging algorithm; and (d) reconstructed image using conventional TFM (for (c) and (d), *Z* axis represents the distance below the array surface which is positioned at *Z*=0; *X* axis represents the distance in RoI only (dotted-line-framed region in Fig. 6(a))

In the RoI images, each SDH in the two specimens is precisely depicted, showing not only its location and upper surface, but also its lower surface, thanks to inclusion of multiple wave reflections from the damage and from the specimen bottom during wavefield extrapolation in the proposed approach. Notably, the proposed ASA allows imaging of the RoI only, while avoids modeling and imaging the entire fluid–solid coupled system, which significantly reduces computational cost and unburdens computing hardware.

Artifacts are observed in the reconstructed images, most of which are near the specimen upper surfaces – an inevitable consequence due to the inclusion of wave reflections from the specimen upper surface during wavefield extrapolation. Upon obtainment of the wavefields at the interface, the reflection remains in the incident wave to the specimen, and then in the backward propagation, resulting in artifacts near the specimen upper surfaces.

4. Discussion: Comparison with Conventional TFM

To compare with the proposed RTM-based multistep ASA, conventional TFM is recalled, to characterize the same SDHs in the two specimens, in which all testing parameters remain unchanged. In the conventional TFM-based imaging, wave reflections from the specimen bottom are not considered. With the determined locations of the specimen upper surfaces, ToFs of waves are extracted from captured signals, with which images of the specimens are reconstructed, in **Fig. 5(d)** and **6(d)**. In the reconstructed images, all SDHs are located, whereas the image resolution is fairly low with inadequate description of SDHs, and in particular the lower surface of each SDH is not depicted. In comparison with the conventional TFM, the RTM-based multistep ASA has proven capability of defining the lower damage surface with obviously improved image resolution. In conventional TFM, the irregular specimen surface is also a barrier to preclude the time-reversed signals from focusing at the damage location, resulting in low imaging resolution. Artifacts are also observed in TFM-reconstructed images, which can be attributed to the multiple wave reflections between specimen bottom and the damage.

Figure 7 further compares the mean values of the image pixel within the depth of $\pm 0.5\,\text{mm}$ where SDHs exist, obtained using the proposed multistep ASA approach and using the conventional TFM-based algorithm. To facilitate comparison, imaging contrast is defined, which calibrates the difference between the peak value of the reconstructed SDH and that of the background. It is clear that the background value is reduced remarkably using the proposed ASA-based algorithm. The imaging contrast value obtained using the ASA-based algorithm is observed as high as 1.5 times the value yielded using TFM for the first specimen, **Fig. 7(a)** and 2 times the value for the second specimen, **Fig. 7(b)**.

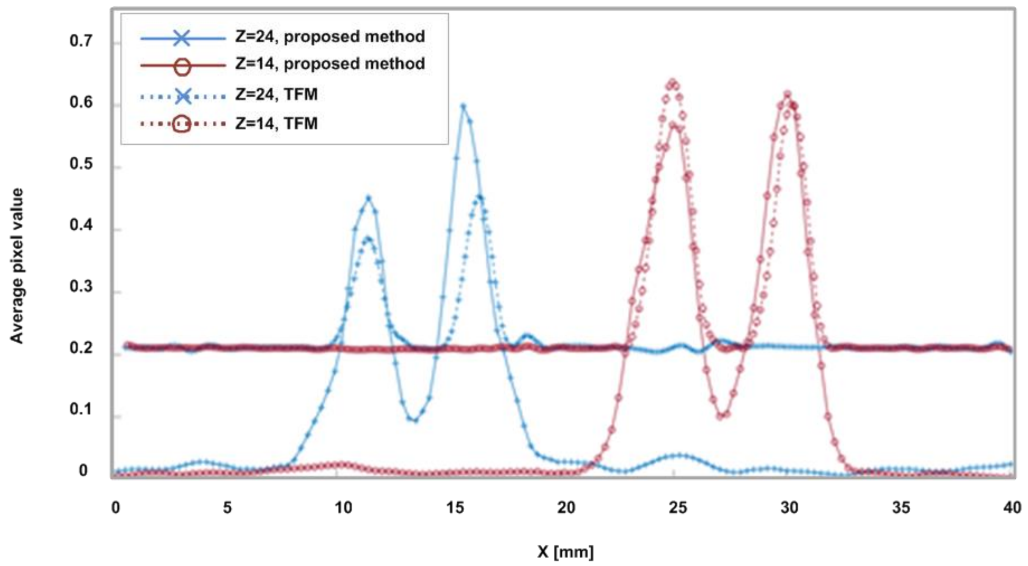

(a)

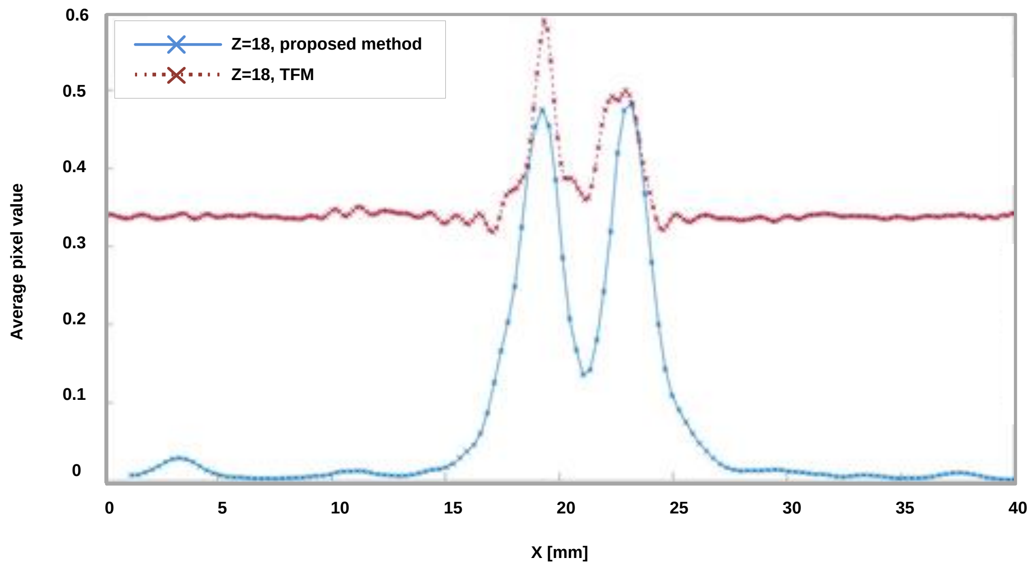

(b)

Fig. 7. Average values of image pixel within the range of ±0.5 mm near SDHs: (a) when z = 14 and 24 mm for the specimen with a parabolic curve; and when (b) z = 18 mm for the specimen with a sinusoidal surface

Although the image resolution of TFM-based or RTM-based imaging does not, in theory, tend to downgrade as depth increases, the quality of reconstructed images may deteriorate due to ultrasonic wave attenuation. **Figure 7** argues that the multistep ASA evidently suffers less than TFM from such influence due to wave attenuation, and remains higher image quality for damage at a deeper depth. Such a merit is attributable to the fact that the reflections from the specimen bottom are considered in the wavefield extrapolation.

5. Concluding Remarks

An RTM-based multistep ASA imaging framework is developed for non-destructive testing of a specimen featuring an irregular top surface via water immersion. Multistep ASA calculates forward propagation wavefields of sources and backward propagation wavefields of the received wave signals in the fluid–solid coupled system, with which the transient wavefields at the fluid–solid interface are used as incident waves to the solid. Thanks to the RTM-enhanced algorithm in which multiple wave reflections from the specimen bottom are taken into calculation, the proposed approach demonstrates its capacity of accurately depicting the lower surfaces of multiple damages hidden in the specimen. Numerical simulation and experiment are performed to validate the proposed approach, in both of which multiple SDHs, at different locations in aluminum blocks with various irregular surfaces, are characterized quantitatively. The validation affirms that the multistep ASA shows higher computational efficiency, compared to conventional RTM, and an enhanced imaging contrast against prevailing total focusing methods.

Acknowledgments

The work was supported by a General Project (No. 51875492) and a Key Project (No. 51635008) received from the National Natural Science Foundation of China. Z Su acknowledges the support from the Hong Kong Research Grants Council via General Research Funds (Nos. 15202820, 15204419 and 15212417).

References

[1] B.W. Drinkwater, P.D. Wilcox, Ultrasonic arrays for non-destructive evaluation: A review, NDT&E Int. 39 (2006) 525-541.

[2] N. Portzgen, D. Gisolf, G. Blacquiere, Inverse wave field extrapolation: A different NDI approach to imaging damages, IEEE Trans. Ultrason. Ferroelectr. Freq. Control 54 (1) (2007) 118-127.

[3] Z. Bai, S. Chen, L. Jia, Z. Zeng, Phased array ultrasonic signal compressive detection in low-pressure turbine disc, NDT&E Int. 89 (2017) 1-13.

[4] Z. Han, H. Peng, P. Lu, 3D ultrasound imaging in frequency domain with 1D array transducer, Ultrasonics 76 (2017) 28-34.

[5] K. Nakahata, S. Tokumasu, A. Sakai, Y. Iwata, K. Ohira, Y. Ogura, Ultrasonic imaging using signal post-processing for a flexible array transducer, NDT&E Int. 82 (2016) 13-25.

[6] A. J. Hunter, B. W. Drinkwater, P. D. Wilcox, Autofocusing ultrasonic imagery for non-destructive testing and evaluation of specimens with complicated geometries, NDT&E Int. 43 (2) (2010) 78-85.

[7] J. Russell, R. Long, P. Cawley, N. Habgood, Inspection of components with irregular surfaces using a conformable ultrasonic phased array, AIP Conference Proceedings, 1096 (1) (2009) 792-799.

[8] T. Olofsson, Phase shift migration for imaging layered objects and objects immersed in water, IEEE Trans. Ultrason. Ferroelectr. Freq. Control 57 (11) (2010) 2522-2530.

[9] J.G. McKee, R.L.T. Bevan, P.D. Wilcox, R.E. Malkin, Volumetric imaging through a doubly-curved surface using a 2D phased array, NDT&E Int. 113 (2020) 102260.

[10] J. Zhang, B. W. Drinkwater, P. D. Wilcox, A. J. Hunter, Damage detection using ultrasonic arrays: The multi-mode total focusing method, NDT&E Int. 3 (2) (2010) 123-133.

[11] L. Le Jeune, S. Robert, E. L. Villaverde, C. Prada, Plane Wave Imaging for ultrasonic

non-destructive testing: Generalization to multimodal imaging, Ultrasonics 64 (2016) 128-138.

[12] M. Weston, P. Mudge, C. Davis, A. Peyton, Time efficient auto-focussing algorithms for ultrasonic inspection of dual-layered media using full matrix capture, NDT&E Int. 47 (2012) 43-50.

[13] J. N. Potter, P. D. Wilcox, A. J. Croxford, Diffuse field full matrix capture for near surface ultrasonic imaging, Ultrasonics 82 (2018) 44-48.

[14] J. F. Cruza, J. Camacho, Total Focusing Method with Virtual Sources in the Presence of Unknown Geometry Interfaces, IEEE Trans. Ultrason. Ferroelectr. Freq. Control 63 (10) (2016) 1581-1592.

[15] E. Hoyle, M. Sutcliffe, P. Charlton, J. Rees, Virtual source aperture imaging with auto-focusing of unknown complex geometry through dual layered media, NDT&E Int. 98 (2018) 55-62.

[16] M. Sutcliffe, M. Weston, P. Charlton, K. Donne, B. Wright, I. Cooper, Full matrix capture with time-efficient auto-focusing of unknown geometry through dual-layered media, Insight-Non-Destructive Testing and Condition Monitoring 55 (6) (2013) 297-301.

[17] J. Camacho, J. F. Cruza, Auto-focused virtual source imaging with arbitrarily shaped interfaces, IEEE Trans. Ultrason. Ferroelectr. Freq. Control 62 (11) (2015) 1944-1956.

[18] R. Sun, G. A. McMechan, Scalar reverse-time depth migration of prestack elastic seismic data, Geophysics, 66 (5) (2001) 1519-1527.

[19] L. Zhou, F. G. Yuan, W. J. Meng, A pre-stack migration method for damage identification in composite structures, Smart Struct. Syst. 3 (4) (2007) 439-454.

[20] X. Lin, F. G. Yuan, (2001). Damage detection of a plate using migration technique, J. Intel. Mat. Syst. Str. 12 (7) (2001) 469-482.

[21] L. Wang, F. G. Yuan, Damage identification in a composite plate using prestack reverse-

time migration technique, Struct. Health Monit. 4 (3) (2005) 195-211.

[22] X. Lin, F. G. Yuan, Experimental study applying a migration technique in structural health monitoring, Struct. Health Monit. 4 (4) (2005) 341-353.

[23] J. He, F.-G. Yuan, Lamb-wave-based two-dimensional areal scan damage imaging using reverse-time migration with a normalized zero-lag cross-correlation imaging condition, Structural Health Monitoring, 16 (2017) 444-457.

[24] J. He, C.A. Leckey, P.E. Leser, W.P. Leser, Multi-mode reverse time migration damage imaging using ultrasonic guided waves, Ultrasonics, 94 (2019) 319-331.

[25] J. He, D.C. Rocha, P.E. Leser, P. Sava, W.P. Leser, Least-squares reverse time migration (LSRTM) for damage imaging using Lamb waves, Smart Materials and Structures, 28 (2019) 065010.

[26] X. Gao, J. Li, J. Ma, J. Li, F. Shi, W. Wang, C. Wang, Experimental investigation of the detection and location of a target in layered media by using the TR-RTM mixed method, Sci. China Phys. Mech. 62 (3) (2019) 34311.

[27] B. E. Anderson, M. Griffa, P. Y. L. Bas, T. J. Ulrich, P. A. Johnson, Experimental implementation of reverse time migration for nondestructive evaluation applications, J. Acoust. Soc. Am. 129 (1) (2011) EL8-EL14.

[28] S. Müller, E. Niederleithinger, T. Bohlen, Reverse time migration: A seismic imaging technique applied to synthetic ultrasonic data, Int. J. Geophys. (2012).

[29] Y. Xu, W. Hu, Ultrasonic imaging for appearance of vertical slot by reverse time migration, Acta Phys. Sin. 63 (15) (2014) 154302.

[30] J. Rao, A. Saini, J. Yang, M. Ratassepp, Z. Fan, Ultrasonic imaging of irregularly shaped notches based on elastic reverse time migration, NDT & E International, 107 (2019) 102135.

[31] H. Liu, B. Li, X. Tong, Q. Liu, X. Wang, W. Liu, The issues of prestack reverse time migration and solutions with graphic processing unit implementation, Geophys. Prospect.

60 (5) (2012) 906-918.

[32] W. Sun, L. Y. Fu, Two effective approaches to reduce data storage in reverse time migration, Comput. Geosci. 56 (2013) 69-75.

[33] A. Asadollahi, L. Khazanovich, Analytical reverse time migration: An innovation in imaging of infrastructures using ultrasonic shear waves, Ultrasonics, 88 (2018) 185-192.

[34] D. P. Orofino, P. C. Pedersen, Efficient angular spectrum decomposition of acoustic sources. I. Theory, IEEE Trans. Ultrason. Ferroelectr. Freq. Control 40 (3) (1993) 238-249.

[35] P. Wu, T. Stepinski, Extension of the angular spectrum approach to curved radiators, J. Acoust. Soc. Am. 105 (5) (1999) 2618-2627.

[36] D. Belgroune, J. F. de Belleval, H. Djelouah, A theoretical study of ultrasonic wave transmission through a fluid–solid interface, Ultrasonics, 48 (3) (2008) 220-230.

[37] F. Varray, A. Ramalli, C. Cachard, P. Tortoli, O. Basset, Fundamental and second-harmonic ultrasound field computation of inhomogeneous nonlinear medium with a generalized angular spectrum method, IEEE Trans. Ultrason. Ferroelectr. Freq. Control 58 (7) (2011) 1366-1376.

[38] U. Vyas, D. Christensen, Ultrasound beam simulations in inhomogeneous tissue geometries using the hybrid angular spectrum method, IEEE Trans. Ultrason. Ferroelectr. Freq. Control 59 (6) (2012) 1093-1100.